ADVANCED MATERIALS INTERFACES
Open Access
www.advmatinterfaces.de

Ice-Bridging Frustration by Self-Ejection of Single Droplets Results in Superior Anti-Frosting Surfaces

Nicolò G. Di Novo, Alvise Bagolini,* and Nicola M. Pugno**

Surfaces capable of delaying the frosting passively and facilitating its removal are highly desirable in fields where ice introduces inefficiencies and risks. Coalescence-induced condensation droplets jumping (CICDJ), enabled on highly hydrophobic surfaces, is already exploited to slow down the frosting but it is insufficient to completely eliminate the propagation by ice-bridging. The study shows here how the self-ejection of single condensation droplets can fully frustrate all the ice bridges, resulting in a frost velocity lower than 0.5 µm s^{-1} and thus falling below the current limits of passive surfaces. Arrays of truncated microcones, covered by uniformly hydrophobic nanostructures, enable individual condensation droplets to grow and self-propel toward the top of the microstructures and then to self-eject once a precise volume is reached. The independency of self-ejection on the neighbor droplets allows a fine control of the droplets size and distance distributions and thus the ice-bridging frustration. The truncated microcones with the smallest heads area fraction maximize the percentage of self-ejecting droplets and minimize the frost velocity. The ice bridges frustration also implies a small frost area coverage, highly desirable in aeronautics and thermal machines.

1. Introduction

In agri-food applications, refrigeration systems' efficiency is reduced by the formation of frost and the necessary defrosting cycles.[1–4] In the automotive market, with a growing demand for electric vehicles, the problem of passenger compartment heating in cold climates has arisen, and one solution is in heat pumps whose efficiency is again reduced by the formation of frost.[5,6] Frosting and subsequent ice accretion also affects aircrafts[4,7] and wind turbines,[4] changing their aerodynamic profile with a subsequent efficiency reduction. Given the toxicity of anti-icing and de-icing fluids used in aircrafts[8] and wind turbines, there has been a growing interest in active systems[9] or systems that use waste heat[10] to prevent and remove ice.

In the last decade, research has intensified into passive anti-icing surfaces to complement or potentially replace active anti-icing methods. In particular, the passive anti-icing effect of superhydrophobic surfaces has been studied. These surfaces allow the rebounding and the freezing delay of supercooled droplets due to the reduced solid-liquid contact area and hydrophobic chemistry.[11–14] However, superhydrophobic surfaces exposed to cold and humid environments are not free from the formation of supercooled condensation droplets[15] which may nullify the aforementioned abilities.[16,17]

Moreover, once few droplets freeze by homogeneous or heterogeneous nucleation, the frost propagates through the ice-bridging mechanism[18,19] in a process called condensation frosting, ultimately covering the surface with ice, which makes it hydrophilic.[20,21] Regarding the microscopic process, the supercooled condensation droplets evaporate and their vapor desublimates on nearby frozen droplets, being the saturation pressure of liquid water higher compared to that of ice for temperatures lower than 0 °C. This results in the formation of "ice bridges" growing from the frozen droplets toward the liquid ones. What regulates the average frost propagation velocity are the diameter (d) and distance (l) distributions of the condensation droplets and the surface temperature,[15] while the substrate thermal conductivity is negligible in comparison.[22] A liquid droplet being sufficiently large and/or close to its frozen neighbor will be reached by the ice bridge, freeze rapidly and originate the next bridge; this propagation is relatively fast. If, on the other hand, the drop is relatively small and/or far from its frozen neighbor, it will

N. G. Di Novo, N. M. Pugno
Laboratory of Bioinspired
Bionic
Nano
Meta
Materials & Mechanics
Department of Civil
Environmental and Mechanical Engineering
University of Trento
Via Mesiano, 77, Trento 38123, Italy
E-mail: nicolo.dinovo@unitn.it; nicola.pugno@unitn.it

N. G. Di Novo, A. Bagolini
Sensors and Devices Center
Bruno Kessler Fundation
Via Sommarive 18, Trento 38123, Italy
E-mail: bagolini@fbk.eu

N. M. Pugno
School of Engineering and Materials Science
Queen Mary University of London
Mile End Road, London E1 4NS, UK

The ORCID identification number(s) for the author(s) of this article can be found under https://doi.org/10.1002/admi.202300759

DOI: 10.1002/admi.202300759

completely evaporate before being reached, causing a slowdown of the bridge which will then be only fed by distant drops. When all the nearest neighbors evaporate, an "ice trail" forms in front of the ice bridges. The more the ice trails, the slower the global frost advancement. The bridging parameter $S^* \equiv L/d$ gives an indication of the success or failure of ice bridges in contacting nearby liquid drops: for $S^* \lesssim 1$ the bridge is successful, vice versa for $S^* \gtrsim 1$.[23] L is the distance between the liquid droplet center and the edge of the frozen droplet. The frost velocity is in the order of tens of μm s^{-1} for common surfaces with $S^* \lesssim 1$ for all the droplets.

On the basis of this description, introduced by Boreyko et al.,[24] structured surfaces hydrophobic enough to enable CICDJ[25–29] were investigated and designed for anti-frosting applications.[30–36] Out-of-plane jumps generate droplet populations having smaller average diameter and larger average spacing compared to the typical populations of non-jumping coalescing droplets on hydrophobic or hydrophilic surfaces. The jumps effectively delay the frost propagation as a high percentage of droplets with $S^* \gtrsim 1$ is maintained over time but, at the same time, being the location of droplets random, a residual percentage of droplets with $S^* \lesssim 1$ establishes the lower limit of the frost velocity around some μm s^{-1}.[24,30–36] Alternative anti-frosting strategies are the disposition of the condensation droplets on hydrophilic micropatterns[37] or the use of microstripes that promote ice nucleation and confine frost on them.[38] However, a drawback of such strategies is in the loss of water repellent and anti-icing effects of superhydrophobicity.

We wondered how to realize a superhydrophobic surface capable of suppressing ice-bridging for all the droplets. This aim guided the conceptualization of single droplet self-ejection from truncated microcones with uniform wettability, theoretically described and experimentally demonstrated in our previous study:[39] nucleated Between four microcones, a nucleated droplet grows by condensation until it settles symmetrically. Then, the increasing volume accommodates to maintain a uniform internal pressure by variating the top and bottom menisci contact angles and the contact line position. Its shape is similar to a prolate spheroid and the correspondent surface energy (E_s) is not at its minimum. As the droplet reaches a certain dynamic configuration, it self-propels by releasing E_s. The fast self-propulsion is determined by the driving surface force and the opposing capillary and viscous forces. The droplet accelerates, decelerates and stops at a certain distance dependent on the dynamic angles and the tapering. Then, it continues to grow and the cycle repeats. Once it reaches the top edges of the truncated microcones, it grows to another dynamic configuration and self-ejects completely with a velocity dependent on the structures size, tapering, and dynamic angles. The self-ejection makes the jumps independent from the proximity to other drops and happens at a precise volume given by the microstructures' geometry and dynamic contact angles. Moreover, we proved that micro pinning sites—hydrophilic or less hydrophobic than the surrounding[40,41]—are superfluous for self-ejection, this greatly facilitating the surface fabrication and scalability.

In the present study, we experimentally investigate the anti-frosting effect of the self-ejection phenomenon and how much the head area fraction of the truncated cones (φ_H) influences the percentage of self-ejecting drops and the frosting speed and coverage. The microstructures with the smallest φ_H are the most performing since almost all the drops self-eject (≈90%) and none of the remaining satisfies the condition of successful ice-bridging. All the droplets evaporate completely before being touched and the frost front slowly advances purely by evaporation-desublimation, forming spectacular crystals that resemble snowflakes. As φ_H increases, successful ice-bridging events happen and mix with the pure evaporation-desublimation growth. We here quantify the average speed of the crystals, the global propagation velocity, and the frost coverage, and relate them with the truncated geometry of the microcones. A frost velocity of 0.4–1 μm s^{-1} is demonstrated in the central portion of the sample, on areas of hundreds/thousands of μm^2, while on the full sample scale (1–4 cm^2), where edge effects are influential, it increases to 1–3.5 μm s^{-1}. This novel class of superhydrophobic surfaces establishes a new limit of passive anti-frosting and promises advancements in other applications such as condensation heat transfer, water harvesting and self-cleaning.

2. Experimental Section

2.1. Microstructuring

The surfaces tested here were presented in the previous study[39] on the self-ejection mechanism. Five surfaces (Group1) served for the fabrication process setup, while the other four (Group2) were employed for characterizing the self-ejection transients and final velocity as the droplet radius varies. All consist in arrays of truncated microcones arranged in a square pattern fabricated on 6-inch silicon wafers (100) by photolithography and tapered reactive ion etching (t-RIE). Their surface was uniformly covered by Aluminium nanostructures (NanoAl) obtained by hot water treatment (HWT) and rendered hydrophobic by silanization (**Figure 1**).

The following steps were the same for both the groups: after a standard RCA cleaning, the hard mask was made by growing 200 nm of thermal silicon oxide (Centrotherm E1200HT furnace) followed by the deposition of 200 nm of Aluminium by magnetron sputtering (Eclipse MRC). Then 1.2 μm of positive photoresist was deposited by spin coating (Track SVG). Two photolithographic masks (Photronics) were employed, as described in detail in our previous study:[39] Mask1 for Group1 with patterned areas of 1 cm × 1 cm (mask aligner Suss MA150CC) and Mask2 for Group2 with patterned areas of 2 cm × 10 cm (Nikon stepper model 2205i11D). The masks consist in circles of diameter D_m and pitch p indicated in **Table 1** where each surface is named *Surface*_$D_m \times p$. After developing (Track SVG), hard bake of the photo-polymer was carried out. The pattern-transfer onto the hard mask was performed by dry etching of Aluminium (KFT Metal PlasmaPro100 Cobra300) and Silicon oxide (Tegal 903e). Then the t-RIE step (Figure 1a) was performed (Alcatel dry etcher) with the following parameters: source power 2800 W, bias power 20 W, gas fluxes ratio $SF_6/C_4F_8 = 0.65$, total gas flux 500 sccm, chamber pressure 0.04 mbar and wafer temperature 20 °C. An SEM image after this step is in Figure S1 (Supporting Information). The etching passivation layer was removed by immersion in isopropanol with ultrasonic pulses.

The hard mask removal was different for the two groups. For Group1, HF vapor (PRIMAXX uEtch System) was employed to

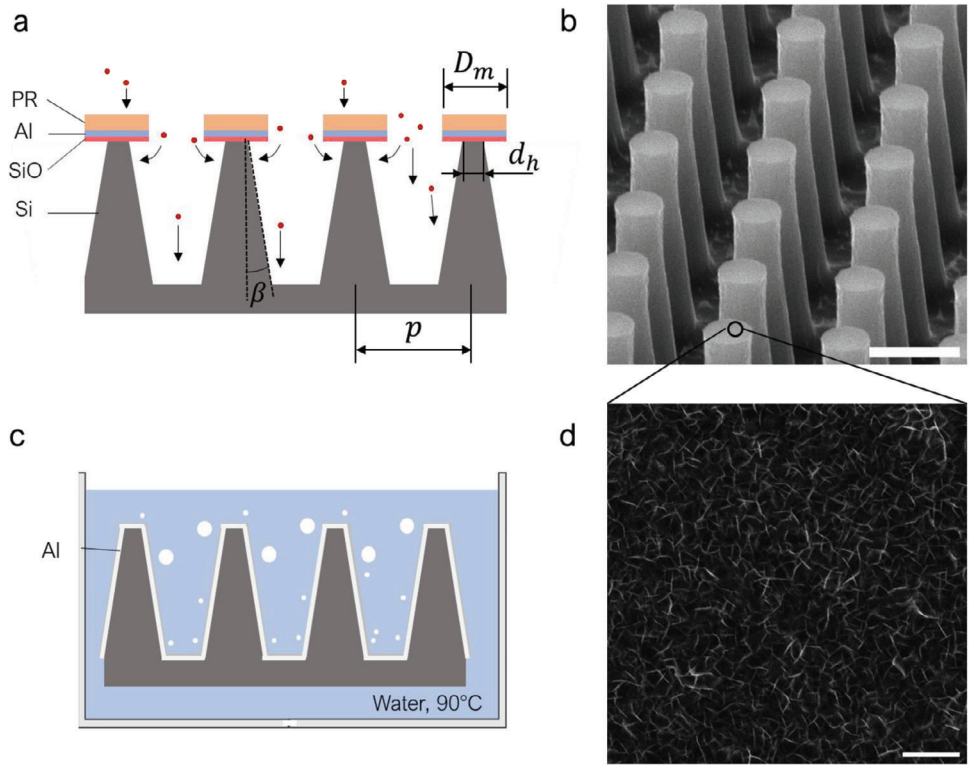

Figure 1. a) Si truncated microcones by tapered reactive ion etching (t-RIE). b) SEM image (tilt angle of 60°) of Surface 10 × 13 after t-RIE and hard mask removal. Scale bar 10 µm. c) Si truncated microcones covered by Al and immersed in hot water to obtain NanoAl. d) SEM image of NanoAl covering the microcones surface. Scale bar 500 nm.

etch the silicon oxide under the Al circles, followed by a jet of deionized water to mechanically remove them. As a result, the hard mask was completely removed from the top of the microstructures but remained on the flat parts of the wafers. For Group2, the hard mask was removed entirely by immersing the wafers in an Al etch solution and then in a silicon oxide etch solution. All the wafers were cleaned in a deionized water rinse until the bath reached 16 MΩ cm. The truncated microcones have a slight undercut at the apex and it was removed with isotropic etching (Tegal 900) that lowered the pillars by ≈2 µm and made the top part straight. An example of truncated microcones after these steps is in Figure 1b.

The tapering β (reported in Table 1 and obtained with the procedure described in Section S2, Supporting Information) was constant from the bottom base up to about three fourths of the microstructure, then it goes to zero in the upper cone portion. In Table 1 All the geometrical parameters measured and calculated by analyzing SEM (Vega3, Tescan) images were reported. A parameter that will be used in the analysis of the performances is the head area percentage (φ_H) defined in

Table 1. Geometry parameters and HWT times of the nine tested surfaces.

Surface name	D_m [µm]	p [µm]	β [°]	d_h [µm]	Height [µm]	φ_H[%]	HWT time [s]
Group 1							
5 × 10	5	10	3.6	1.2	16.4	1.13	450
10 × 15	10	15	4.9	3.9	30.7	5.31	540
10 × 20	10	20	3.5	3.9	29.1	2.98	540
15 × 20bis	15	20	6.2	5.8	41.1	6.61	490
15 × 25	15	25	4.5	5.4	42.0	3.66	490
Group 2							
10 × 13	10	13	6.6	5	23.3	11.62	420
15 × 20	15	20	6.6	7	34.9	9.62	420
30 × 40	30	40	10	12.5	64.3	7.67	420
60 × 80	60	80	8.8	31.5	103.7	12.18	420

Equation 1, where d_h is the head diameter of the truncated microcone.

$$\varphi_H = \left[\frac{\pi}{4}\left(\frac{d_h}{p}\right)^2\right] 100 \quad (1)$$

2.2. Nanostructuring, Silanization, and Contact Angles

As a second hierarchical level covering the truncated microcones, nanostructured Aluminium (NanoAl) obtained by HWT was chosen. The HWT of many metals and their alloys leads to the formation of nanostructures: a thin superficial layer of metal oxide forms in hot water, the oxide cations were released in solution, migrate and deposit forming nanostructures with peculiar shapes for each metal.[42] In the case of Al, thin nano-blades of hydrated aluminium oxide (pseudo-boehmite) form.[43] Once made hydrophobic, these nano-blades gain superhydrophobic and anti-freezing properties.[54–59] 150 nm of pure Al was initially deposited on the truncated microcones by e-beam evaporation (ULVAC HIGH VACUUM COATER EBX-16C). The wafers were cleaved in samples of ≈2 cm × 2 cm for Group2 and in samples of ≈1.3 cm × 1.3 cm for Group1. In order to enable observation of droplet jumps from side-view, Group2 had samples with a row of cones on the sharp edge. HWT was performed by immersion in deionized water (18 MΩ cm) at 90 °C (Figure 1c). As reported,[39] the HWT time of Group2 was 7 min and the darkening, due to nanostructuring, was simultaneously visible on the entire sample and started a few seconds after immersion. The Group 1 samples, as explained, had the micro-patterned area free from the circles of the hard mask, which instead remained as a continuous area outside the patterned area. On preliminary samples processed with the procedure of Group1, a delay of the darkening was noticed during HWT. In particular, it appeared after some tens of seconds, starting from the center of the patterned area——far from the hard mask——and rapidly propagating toward the edges of the patterned area. This observation offered an insight and a useful guideline for NanoAl fabrication. Two pioneering studies of D. A. Vermilyea and W. Vedder, dating back to 1969–70, report the inhibition of aluminium and water reaction by the presence of other compounds, e.g. silicic acid (H_4SiO_4).[43,44] Silicon oxide dissolves in water and forms silicic acid,[45] thus the thin silicon oxide sublayer of the hard mask acts as a retardant of nanostructuring. In order to have a similar nanostructuring between the two groups, we immersed the Group1 samples, waited for the darkening to begin (appreciable to the naked eye) and left 7 min to pass before extraction. Table 1 shows a certain variability of the waiting time that depends on the hard mask flat area fraction. After HWT, the samples of both groups were immediately immersed in room-temperature deionized water to block the nanostructuring and dried with a nitrogen flow. In Figure 1d, the NanoAl covering the surface of the truncated microcones is visible.

The micro and nanostructured surfaces were cleaned by dipping in acetone, isopropanol, and deionized water, dried with a nitrogen flow and activated the surfaces with oxygen plasma. Chemical vapor deposition (CVD) of 1H,1H,2H,2H-Perfluorodecyltriethoxysilane (Sigma–Aldrich) was performed by placing the samples and 200 µL of fluorosilane in a sealed (class IP-67) aluminium box (internal volume of 3.7 L) heated at 150 °C for 3 h, followed by annealing for 1.5 h with the box opened (for covalently unbound silane removal).

The advancing and receding contact angles of microdroplets condensing and evaporating on the NanoAl covered microstructures were evaluated to be ϑ_a = 157 ±1° and ϑ_r = 145 ± 6, respectively.[39]

2.3. Experimental Setup

The condensation frosting experiments were carried out in a custom-built environmental chamber[39] and observed with a digital microscope (Dinolite AM7915MZTL – EDGE) from the top-view window. The field of view for observation of the condensation frosting process was 2724 × 2043 ϵm^2 and always centered in the middle of the patterned area, while for the final frost coverage, the entire sample was observed. The single droplet self-ejection and coalescence induced self-ejection Videos S1–S5 (Supporting Information) were recorded from the side view with a high speed camera (Phantom V640, Vision Research) coupled to a microscopy objective (50X Mitutoyo Plan Apo infinity corrected, long working distance = 13 mm, resolving power = 500 nm, depth of focus = 900 nm) through a tube lens (InfiniTube Ultima). The surfaces were illuminated with a LED light (MULTILED QT, GSVITEC) placed outside the environmental chamber and on the back of the samples with respect to the high-speed camera. For the high frame rate recordings the study set T = 1 °C to avoid icing, more likely caused by the vicinity with the thermal paste. The saturation ratio was set to $s = P_{vap}/P_{vap,sat}(T_{surf}) = 2.8$ where P_{vap} is the water vapor pressure and $P_{vap,sat}(T_{surf})$ is the saturation vapor pressure at T_{surf} as for the condensation frosting experiments described in the following.

The plate temperature of the condensation frosting experiments was set to $T_p = -11$ °C. The sample and the temperature sensor (thin film PT100 thermocouple, RS pro, class B accuracy) were in thermal contact with the cold plate through a thermal pad (T-flex 600 Series Thermal Gap Filler, Laird Technologies, thickness of 1 mm, thermal conductivity of 3 W mK^{-1}). Given the low thermal inertia of the silicon samples (600 µm thick) and of the PT100, it is assumed that surface temperature $T_{surf} \cong T_p$. All the frosting experiments were performed with samples positioned vertically so that jumping droplets that fall back to the surface were minimized. To assure the desired T_{surf} from the beginning of the experiments, the thermal pad positioned on the plate at room temperature, the samples were pressed on the pad from the edges, the chamber was then closed, and dry air was flushed until the vapor pressure inside the chamber fellbelow the saturation value, corresponding to −11 °C. Then the T_{surf} was lowered to −11 °C, humid air with a P_{vap} = 7.4 hPa was fluxed and recording started. Within a few seconds, the first condensation nuclei appeared.

2.4. Self-Ejection Percentage and L/d Distributions

The effectiveness of all the surfaces was evaluated in self-ejecting condensation droplets belonging to the first generation of nucleated droplets. For the Videos S6–S9 (Supporting Information)

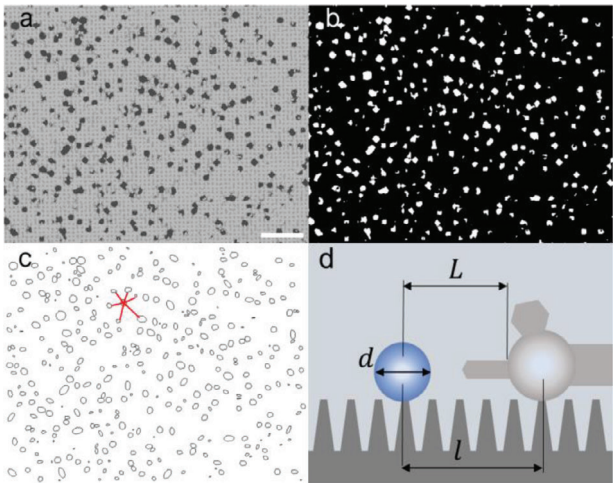

Figure 2. a–c) Sequence of the image analysis procedure performed with ImageJ of the Surface_10 × 20. Red lines in (c) are an example of the calculations done by the code. The Analyze particles plugin fit each droplet with an ellipse. Each droplet radius is calculated as the mean of the two axes of the ellipse. Scale bar is 200 µm. d) Scheme of an ice bridge growing from a frozen droplet to a liquid one on top of the truncated microcones with L and d indicated.

with field of view of 2724 × 2043 ϵm^2 the frames were extracted and analyzed 3–4 square sub-zones having a size of 500–800 µm. By counting the number of self-ejected droplets and the total number of nucleated droplets we obtained the percentage of self-ejecting droplets ($\%_{s-ej}$). Every droplet nucleated on lateral walls or on the bottom self-ejects. The ones on top of the truncated cones, which cannot self-eject, grow until they coalesce with other droplets on top or between the cones and jump off the surface. The $\%_{s-ej}$ of Surface_5 × 10 was not evaluated for uncertainties related to the microscope resolution, but self-ejection was observed.

The droplet population of the most performant surface (10 × 20) was analyzed to support the key idea of ice-bridging frustration by self-ejection. ImageJ's plugin Trainable Weka Segmentation[46] was used to classify the images into "droplets" and "substrate" classes (**Figure 2a**). The Smooth, Threshold, and Irregular watershed plug-in were applied (Figure 2b) and then Analyze particles to quantify the diameter and position of each droplet (Figure 2c). The output was passed to a plugin for calculating the average size and distance between particles and their closest neighbors.[47] The plugin was modified to calculate L/d for each drop, averaged over the six nearest neighbors. L and d are depicted in Figure 2d, in accordance with the literature.[23] The normalized distribution of L/d over the entire population was a sort of probability density function of a drop being touched by ice bridges coming from its closest frozen neighbors. The average distance (between the centers) of each droplet was also extracted with its six neighbors and the diameter distributions.

2.5. Frost Velocity and Coverage

In the literature there are several ways to measure the speed of frost propagation (v_{frost}), not equivalent. To calculate v_{frost} on observation windows of few hundreds of microns, some authors divided either the length[24] or the diagonal[48] or the square root of the area[33] by the time in which all droplets in the observed area are frozen (frost velocity of the order of tens of µm s^{-1}). Other authors, quantified the frosting rapidity as an area covered by frost per second (µm2 s^{-1}).[34,49] Others divided the area per second by the perimeter of the frost front (µm s^{-1}).[32,50] In the experiments with a large field of view (2783 µm × 2087 µm), several fronts with different velocities were observed (non homogeneous spreading). The faster fronts follow paths along where S is the smallest. In the other zones where $S \gg 1$ the droplets completely evaporate, an extended dry zone forms and the propagation velocity is negligible in comparison. For each experiment, some (3–6) directions were identified along which the dendritic/ice-bridging front grew faster, measured their length (l) every 100 s, calculated their instantaneous velocity as $v = l/100s$ and the temporal mean v_t. v_{frost} was calculated as the mean of the various v_t. v_{frost} was calculated using only the faster fronts because they determine the millimetric scale connections between frost fronts that start from different ice nucleation sites. Those connections are the weak link for the anti-frosting and anti-icing properties of a surface, e.g. the repellence to supercooled impacting droplets that requires a frost-free large area. Indeed, as it will be shown, v_{frost} is specific of the droplets population and not of the ice nucleation sites density ($\rho_{n,i}$) that can be affected by other parameters like impurities, surface defects and environmental conditions.[51] Important to note, v_{frost} evaluated with the method is, at best, higher compared to the values obtained with other methods. Thus, it can be safely said that the present surfaces overcome the current limits.

The global frost velocity v_{glob} was also calculated as the square root of the total patterned area of a sample divided by the time after which all the droplets are frozen, t_{frost}. The relation between v_{glob}, $\rho_{n,i}$ and v_{frost} will be discussed.

Trainable Weka Segmentation was used to classify the images into "frost" at the end of the propagation and "substrate" classes and then Analyze Particles to quantify the fraction of the area covered by frost. The frosted area percentage was evaluated for both the 2724 × 2043 ϵm2 field of view in the center of the sample ($A_{f,\,local}$) and at the scale of the entire sample ($A_{f,\,glob}$).

3. Results and Discussion

3.1. Self-Ejection and $\%_{s-ej}$ Versus φ_H

The self-ejection timeline is represented in **Figure 3a**. As stated in the introduction and analyzed in our previous study,[39] the droplet nucleates and slowly grows between the cones by accommodating the condensation volume in isopressure configurations. Once it reaches a dynamic configuration, it self-propels rapidly driven by surfaces energy release and stops at a certain distance. Between $t = 1$ and $t = 4$, the droplet alternates slow growths and rapid self-propulsions . When it reaches the truncated cone edges, it slowly grows to another dynamic configuration ($t = 4$) and then rapidly self-ejects by releasing surface energy (between $t = 4$ and $t = 5$). The peculiarity of the present structures is that self-ejection starts without an abrupt detachment of the droplet from the base of the structures or from a inserted pinning site.[40,52] It is purely a release of surface energy once a dynamic configuration is achieved. Figure 3b reports the self-ejection event shown in Video S1 (Supporting Information). The

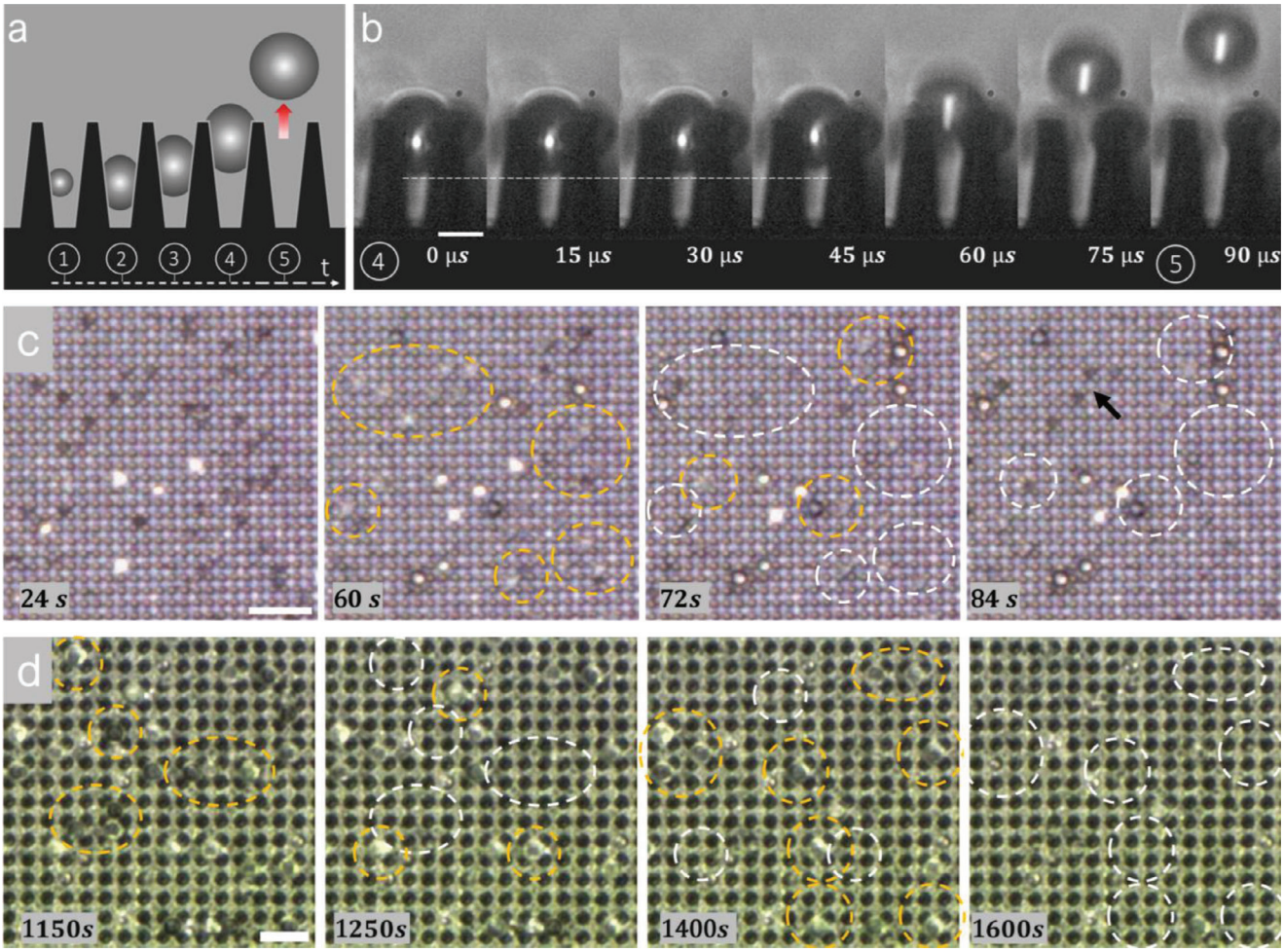

Figure 3. a) The timeline of a condensation droplet from nucleation to self-ejection. The droplet 1) nucleates, 2) settles between the four cones and grows to the dynamic configuration, 3) alternates fast self-propulsions to slow growths until it reaches the top of the truncated cones and 4) grows to a self-ejection dynamic configuration. From 4) to 5) it self-ejects as captured in b) in tens or hundreds of microseconds depending on the structures' size, while from phase 1) to 4) it can take tens of seconds to minutes. The captured droplet self-ejects from Surface_10 × 13 cooled to 1°C and in a atmosphere with saturation ratio equal to 2.8. Scale bar is 10 μm. c) Top view experiment of the Surface_15 × 20p. The dotted yellow ellipses indicate where self-ejection is going to occur and the white ones in the next frame where droplets self-ejected. The dark zone indicated by the black arrow at 84 s are re-nucleation sites. The time displayed refers to the beginning of the video that coincides with the introduction of humid air. Scale bar is 100 μm. d) Self-ejection events from Surface_30 × 40. Scale bar is 100 μm. Experiments of c,d) where done at T = −11 °C and saturation ratio 2.8.

gradual acceleration of the droplet is more evident in the Video S2 (Supporting Information) capturing a self-ejection droplet from Surface_60 × 80.

In Figure 3c,d we report two examples of top-view recordings (see Videos S6 and S7, Supporting Information). Every droplet self-ejects if it nucleated on the side-walls or bottoms of the truncated cones, while the ones on the heads of the cones can only jump off due to CICDJ. **Figure 4** reports the $\%_{s-ej}$ as φ_H varies for all the surfaces. The trend confirms this description: the higher φ_H, the fewer the self-ejections. The red dot represents Surface_60 × 80 and its small $\%_{s-ej}$ is discussed in the next paragraph. Thanks to self-ejection, the few droplets on the heads of the microcones are very spaced and rarely as large to have $S^* \lesssim 1$ also because they can jump by coalescing with other droplets (which will be discussed in the next paragraph). Large droplets spacing and small diameters implies $S^* > 1$ for every droplet and thus frustration of ice bridges.

The slightly different nanostructuring procedure between Group1 and Group2 has no effect on enabling self-ejection and thus on the relations with φ_H analyzed in the present work; apart from those nucleated on the heads, every droplet self-ejects.

3.2. Other jumping modes

After self-ejection there are two possibilities:

1) droplets re-nucleate on the same site, grow and self-eject; the cycle repeats.
2) the old nucleation site remains free, and condensation accumulates on neighboring droplets placed between or on top of the cones.

After a certain time dependingon cone spacing, and therefore on the time to achieve the self-ejection volume, the remaining

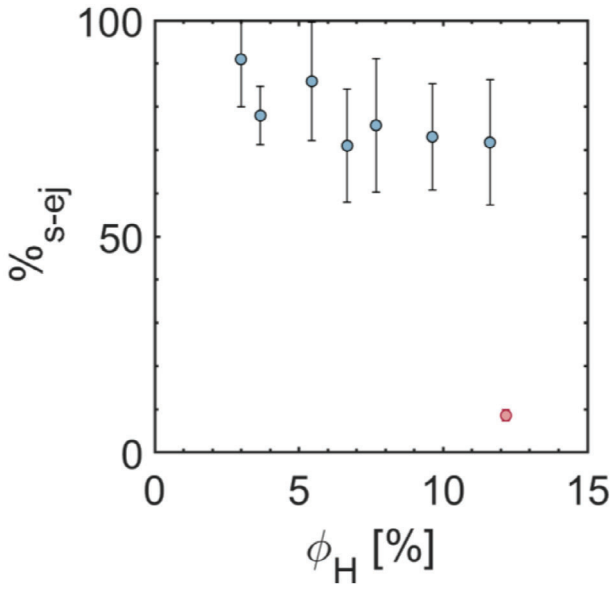

Figure 4. Percentage of self-ejecting droplets ($\%_{s-ej}$) with respect to the total number of droplets nucleated as the head area percentage, φ_H, varies.

droplets are only those nucleated on the heads of the cones. In the case of a vertical surface, they can leave the surface in 3 ways: they coalesce either i) with other drops on top of the heads or ii) with those located between the cones that grow and self-propel toward the aperture (see **Figure** 5a, an event captured in slow motion), or iii) they are swept away by droplets located between the cones in adjacent unit cells that coalesce and eject (Figure 5b). For completeness, we performed some experiments placing the surfaces horizontally: droplets that fall back after self-ejection or CICDJ will trigger other cascading ejections induced by coalescence (Figure 5c). The events of Figure 5a–c are reported in the Videos S3–S5 (Supporting Information), respectively.

Surface_60 × 80 (with the highest φ_H, reported in Figure 5c) is an exception compared to the other surfaces because frost freezes the majority of drops before they can reach the self-ejection volume; however, there were coalescence jumps (of the various types presented above) which in this case are more frequent than on the other surfaces and begin before self-ejection. To avoid frost and give a value to the $\%_{s-ej}$ we tested the surface with $s = 2.8$ but at 1 °C: it corresponds to the red dot in Figure 4. $\%_{s-ej}$ is <10% and coalescence jumping is predominant. This is due to the number of condensate nuclei per unit area being greater than the unit cells per unit area. As a result, the majority of droplets growing inside a unit cell coalesce with others and jump off instead of undergoing self-ejection. Thus, to maximise self-ejection for a large spectrum of saturation ratio one should design the smaller microstructures possible, compatibly with self-ejection requirements.

3.3. Frost Velocity

The most performant surfaces (Surface_5 × 10 and Surface_10 × 20 in **Figures** 6a and 7a, respectively) correspond to the higher $\%_{s-ej}$; as soon as a drop spontaneously freezes in the field of view or the frost front arrives from outside it, all the drops completely evaporate and the frost advances with dendritic formations by desublimation. The crystals are strongly anisotropic because certain facets grow faster than others.

A clear example is in Figure 7a (see Video S8, Supporting Information): the two initial ice crystals (blue and red arrows) have an elongated shape; the short side grows more "rapidly" toward the drops while the long one is much slower (about one third) and forms a large dry zone. The slow facets are not considered in the calculation of v. Moreover, the fast side has a typical slow down of v as the dry zone develops (as also in Figure 6). The two long dendrites developed after ≈5000 s (yellow arrow in Figure 7a) are instead more branched, faster and maintain their speed. In fact, they determine the complete evaporation of the remaining condensation. However, also for the branched dendrites successful ice-bridging was not observed. Therefore the v evolution depends also on the crystal shape (Figure 7b). As shown in Kenneth G. Libbrecht's *Snow Crystals*,[53] the shape and growth rate of ice crystals depends on various parameters such as temperature and saturation ratio. As the temperature is constant during the experiments, we deduce that the saturation ratio is altered in the yellow arrow zone by the presence of large dry zones and frost, because they change the distribution of vapor fluxes from the surrounding air.

On other surfaces with larger φ_H and smaller $\%_{s-ej}$, we instead observed a mixed behavior, i.e., both ice-bridging and the formation of dry zones (see Figure 7c; the correspondent Video S9, Supporting Information). This can be seen from the v of various paths in Figure 7d: unlike the cases with full ice-bridge frustration where velocity steadily decreases, in the mixed behavior it oscillates.

Self-ejection has a superior anti-frosting effect compared to (CICDJ) alone because each droplet jump is independent on the neighbor droplets. The illustrations in **Figure** 8a,b depict the condensation frosting on surfaces that enable self-ejection: the majority of droplets leave the surface as soon as they reach the self-ejection volume and the remaining ones, on the microcones' heads, are far from each other and evaporate completely due to the presence of ice crystals. Thus, the ice-bridging propagation mechanism is frustrated.

Let's suppose a certain number of condensation nuclei per unit area, the density ρ_c, higher than the four-microcones unit cell density, so that for each cell there is a maximum of one droplet. Assuming a population of equally spaced drops, let's estimate the mean distance between the droplets centers as $l_c \sim \sqrt{1/\rho_c}$. Assuming that for very small φ_H, $\%_{s-ej} \to 100\%$; each condensation droplet self-ejects at a precise diameter D_{ej}. This diameter is dependent on the size, tapering and dynamic angles of the microstructures,[39] which also define the maximum droplet diameter D_{ej}. Considering the dimensions depicted in Figure 2d, re-adapted to the case of droplets between the cones and in the most favorable scenario for successful ice-bridging (at the time of maximum diameter, D_{ej}), $L \sim l_c - D_{ej}/2$. By imposing $S^* \equiv L/D_{ej} > 1$, we obtain the criterion $D_{ej} \lesssim 2l_c/3$. Therefore, for a certain ρ_c, dependent on the environmental conditions and on the surface roughness and chemistry, there is a critical self-ejection diameter $D^*_{ej} = 2l_c/3$, tuneable in the design process, under which all the ice bridges fail.

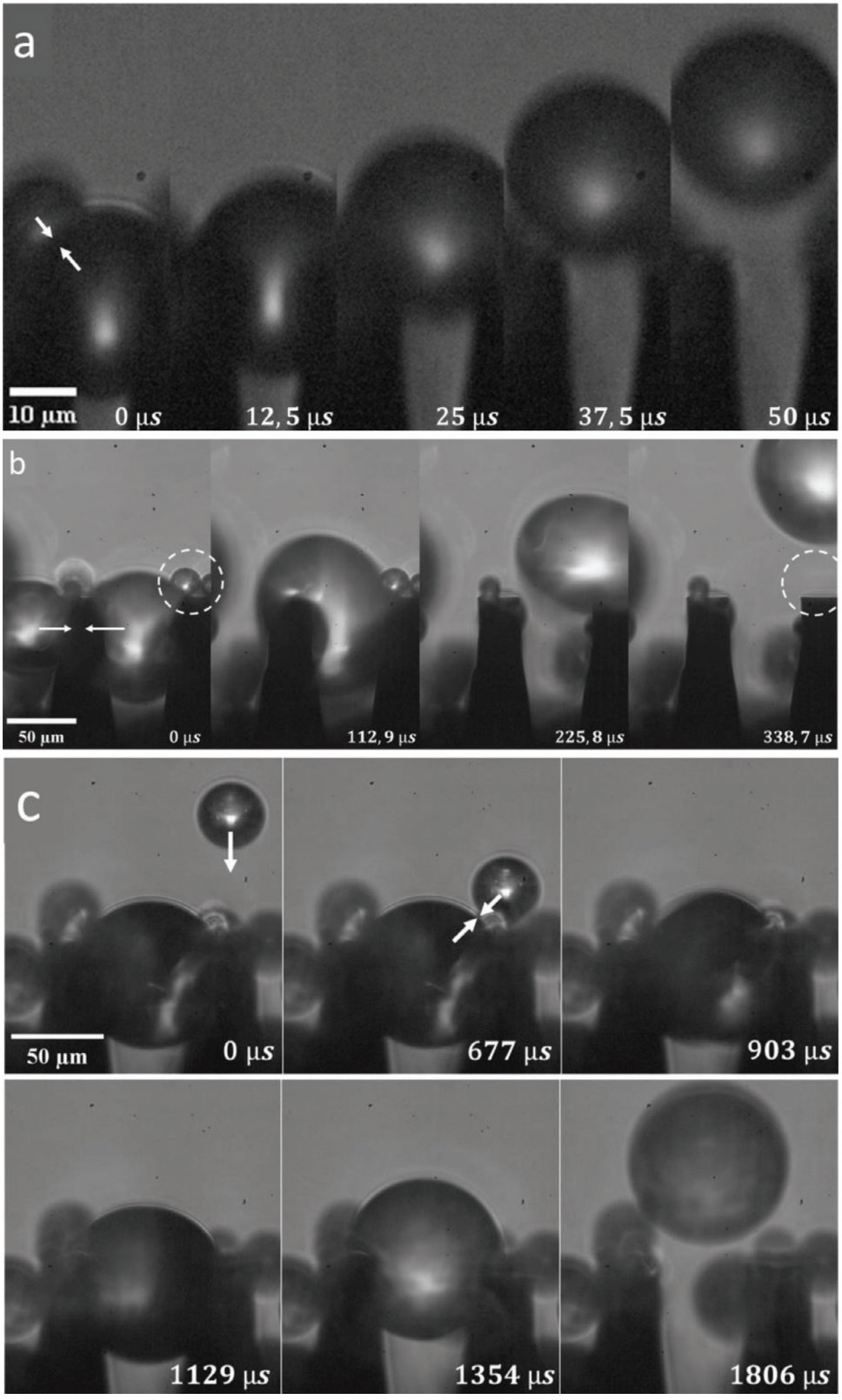

Figure 5. a) Ejection of a droplet located between the microcones induced by coalescence with a droplet on top (Surface_15 × 20). b) Coalescence and ejection of two droplets located between the microcones that also swept away two droplets on top of the right cone (Surface_60 × 80). a,b) are typical jumping modes alternative to self-ejection that happen on vertical surfaces. c) Additional jumping mode on Surface_60 × 80 placed horizontally. Droplets that jumped (due to self-ejection or CICDJ) can fall back on the surface and trigger cascading ejections induced by coalescence.

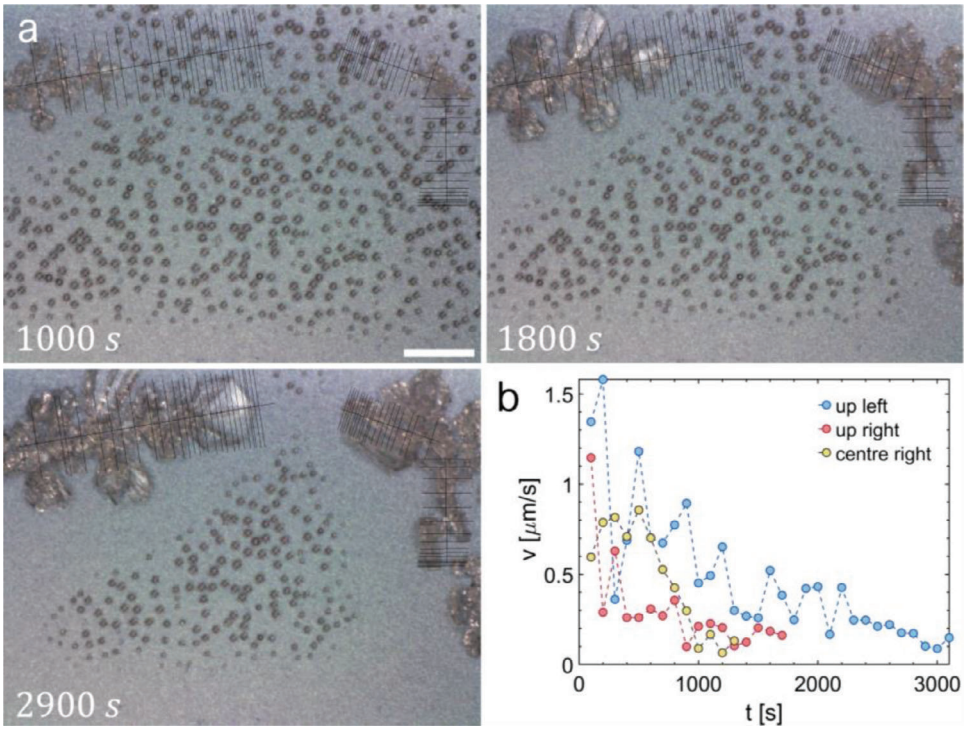

Figure 6. a) Frost dendrites growth on Surface_5 × 10 with the black lines employed to measure v. On this surface, also at the beginning of frosting there was no ice-bridging but complete evaporation of the droplet with the formation of a large depletion zone. At the end of the experiment, the droplets in the middle of the field of view completely evaporated. The scale bar is 400 ϵm. b) v evolution for the three dendrites. It is higher at the beginning because the liquid droplets are closer to ice (the bridge velocity scales as 1/L)[15] while when the dry zone widens it slows down. v_{frost}= 0.42 ± 0.1 μm s^{-1}.

Now let's consider truncated microcones with a certain $\%_{s-ej}$ < 100%; we can consider the droplets in two classes: 1) the self-ejecting ones that assure the ice bridges frustration if the structures are properly designed ($D_{ej} < D^*_{ej}$) and 2) the ones on the heads that can potentially let the frost propagate by contact before they coalesce and jump off. The first generation droplets remaining on the heads have a density $\rho_{c,H} = \rho_c\ (1 - \%_{s-ej}/100)$ and we can say from the experiments (last Section) that it is steady because of the various jumping interactions with the droplets of subsequent generations. The mean distance between their centers becomes $l_{c,H} \sim \sqrt{1/\rho_{c,H}}$. Thus, the larger the $\%_{s-ej}$ (or, in other words, the smaller the φ_H), the larger the $l_{c,H}$ and the mean S^*. In the last Section we shall show that $S^* > 1$ for all the droplets on one of the most performant surfaces.

By plotting v_{frost} as φ_H varies (Figure 8c), we see again an approximately linear dependence which is implicitly affected by the $\%_{s-ej}$, as explained. For surfaces with the highest $\%_{s-ej}$, we recorded the lowest frost velocities.

v_{glob} is at least $2v_{frost}$ as there are multiple fronts advancing in opposite directions starting from the edges of the patterned sample, where there are defects and ice forms quickly because of the hydrophilic plate. On a ideally infinite array of nanostructured truncated microcones (to neglect sample edges), with the presence of ice nuclei distributed with a mean distance $l_{n,i} \sim \sqrt{1/\rho_{n,i}}$, one can estimate the frosting time as $t_{frost} \gtrsim l_n$,i/2v_{frost}, where the equal stands for the (rare) simultaneous appearance of the nuclei. In the presence of icephilic edges of a sample of size l_s and no other ice nuclei, $t_{frost} \sim l_s/2v_{frost}$. In summary, v_{frost} is a specific quantity referred to the propagation from one ice nucleation site toward a population of jumping droplets (self-ejection and CICDJ) while v_{glob} is instead a quantity dependent on both v_{frost} and l_n,i. In our experiments, the dendrites extends for several hundreds of microns and it is representative to compare v_{frost} with the state of art studies cited that report the frost velocity relative to smaller areas, with a side length of a few hundred microns. We can conclude that our best self-ejection enabling surfaces cause frost to propagate 3–11 times slower than state-of-the-art surfaces (Figure 8d). However, (T_{surf}, s) pairs in Figure 8d are not identical. It should be noted that, in general, v_{frost} increases as T_{surf} decreases (higher bridge velocity) and as s increases considerably (closer droplets). The superiority is therefore assured compared to Refs. [24,31,46] while it should be verified for the conditions of the other studies. The advantage of frustrating all ice bridges remains, which is not reported in the literature. As shown in the following section, the consequence of complete frustration is purely dendritic propagation with very low frost coverage.

3.4. Frost Coverage

Regarding the surface's frost coverage, we still found an improvement due to CICDJ[24,30–36] compared to surfaces that exhibit pure ice-bridging or a frost delay only. As seen in **Figure 9**, $A_{f,\,local}$ goes from 20 to 50% while $A_{f,\,glob}$ goes from 41 to 68%; The edges have an effect on the scale of the entire sample because it can happen

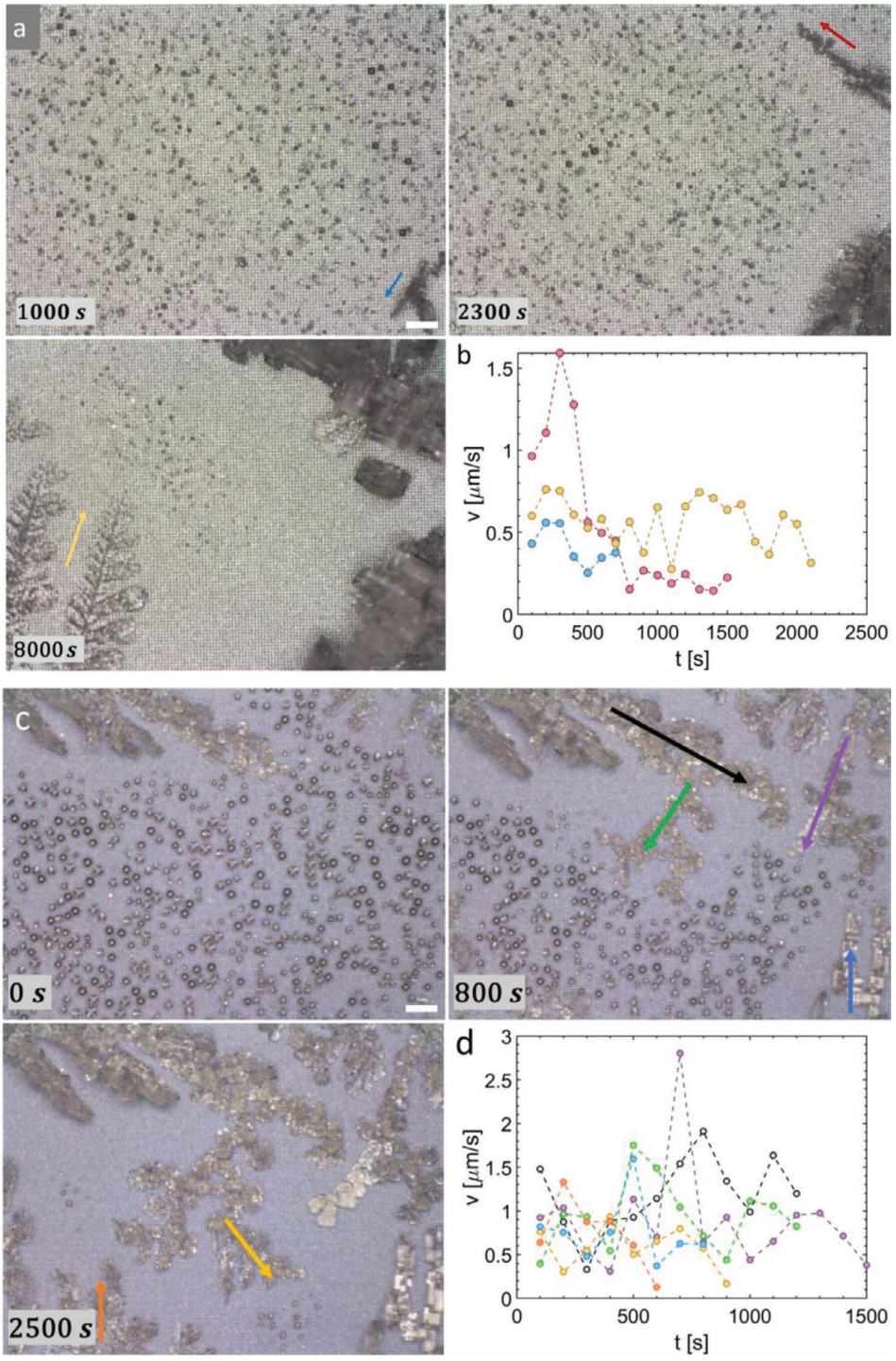

Figure 7. a) Dendrites growth on Surface_10 × 20. Ice-bridging is suppressed for all of them. The fastest fronts are identified by colored arrows. b) v with the correspondent color. We plotted v with the same starting time even if they grow in different time periods. $v_{frost} = 0.50 \pm 0.08$ ϵm/s. c) Surface_10 × 15 with colored arrows correspondent to v in (d). The frost grows with a mixed mode. $v_{frost} = 0.85 \pm 0.21$ ϵm/s. Scale bar 200 ϵm.

that frost starts from there and reaches the drops by ice-bridging before they leave the surface by self-ejection. On larger patterned surfaces we expect $A_{f,\,glob} \rightarrow A_{f,\,local}$. In any case, the free final area is high compared to ice-bridging surfaces or those that exhibit only CICDJ.

Looking for applications, surfaces that exploit self-ejection could improve the efficiency of the heat exchangers where frost coverage is a determining factor. For airplanes, apart from delaying the frosting, a self-ejection enabling surface would have a large area free from frost and still superhydrophobic; supercooled

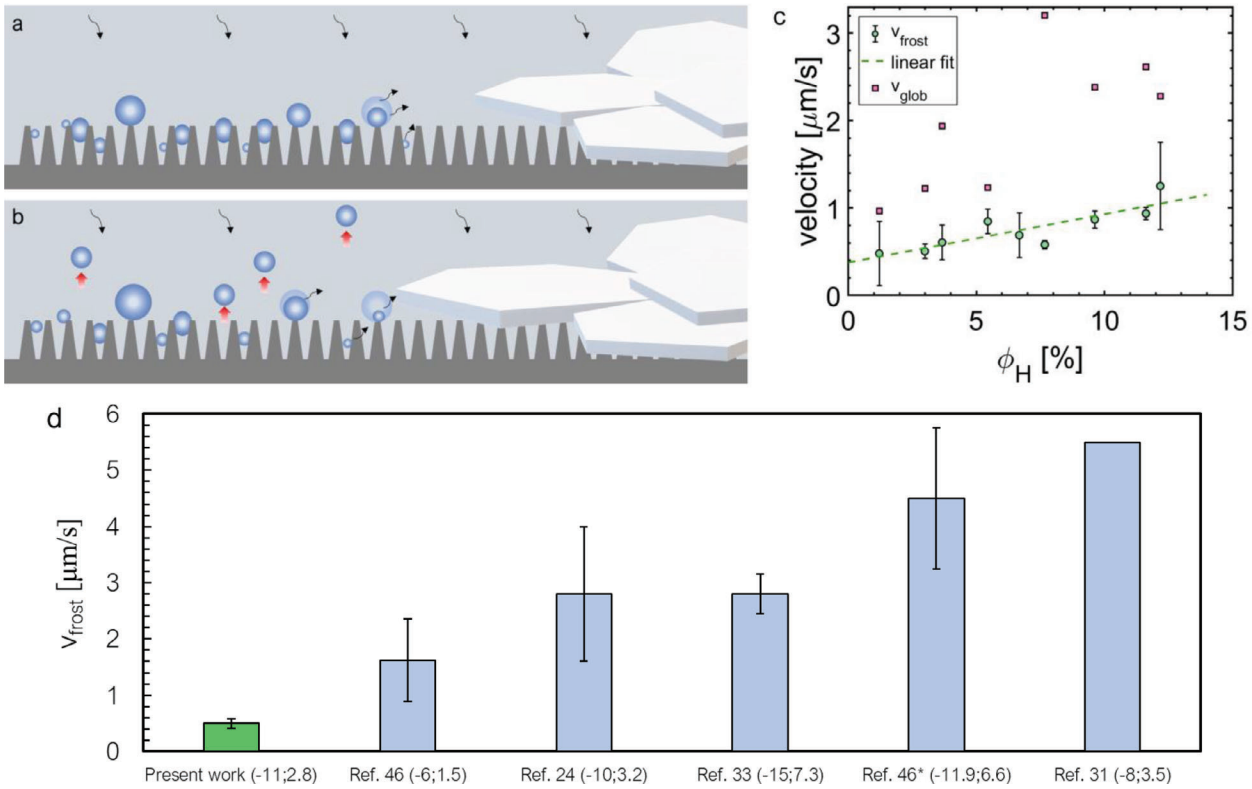

Figure 8. a,b) Illustration of two subsequent times during condensation frosting on nanostructured truncated microcones that enable self-ejection. An high percentage of droplets leave the surfaces at a precise volume and the remaining ones are far enough to evaporate completely before being touched by ice bridges or crystals. c) ν_{frost} and ν_{glob} as φ_H varies. The linear fit is $\nu_{frost} = 0.0554 \cdot \varphi_H + 0.374$ and has a $R^2 = 0.73$. $\nu_{glob} - 2\ \nu_{frost}$ when frost starts form the edges and higher when there are multiple ice nuclei. d) Comparison of the most performant surface from the present study (Surface_10 × 20) with those from cited studies. Each reference provides the surface temperature and saturation ratio, indicated as (T_{surf}; s).

impacting droplets could thus rebound on the free area and wet frost and freeze only. The delamination of the thus formed ice layer (by gravity, wind and other means) would be facilitated because it would have a contact area fraction of $f^* A_{f,\,local}/100$, with f a coefficient defined as the ratio between the real solid-ice area and $A_{f,\,local}$ which is a projected area.

3.5. Ice-Bridging Frustration by Self-Ejection

We verified that the frustration of ice bridging for all the droplets is supported by the condition $S^* > 1$ for all the droplets population. In **Figure 10**a,b we show the normalized distributions of S^* of Surface_10 × 20 at six times in the range 150–3600 s after the beginning of the experiment and before any drop freezes in the field of view. After a few minutes, the drops begin to self-eject in a recurrent way from the same sites, also causing other kinds of jumping (Video S8, Supporting Information). The continuous self-ejections and coalescence-induced jumps of droplets located between and on top of the cones cause the distributions to be stationary, with zero frequency for $S^*<1$. The jumping mode of coalescence of two/more droplets on the head is rare because the coalescence with the ones between the cones is more likely.

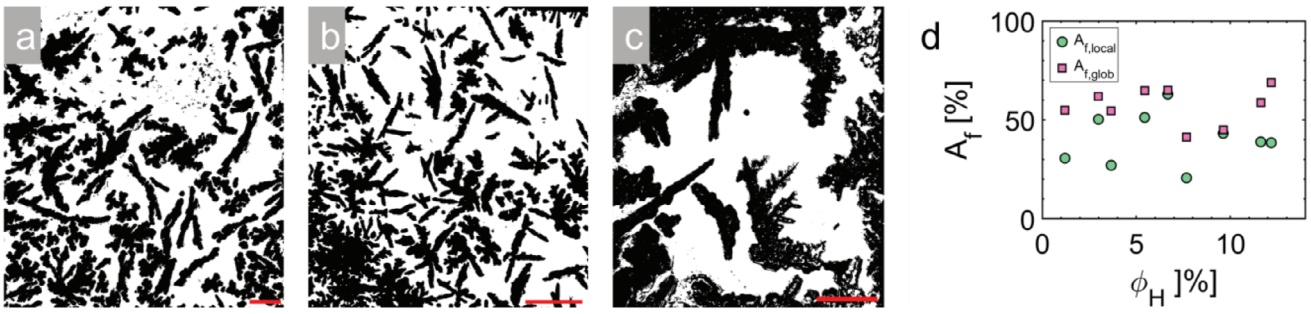

Figure 9. From a) to c), the frost on the patterned area (global) of Surface_15 × 20, Surface_30 × 40, and Surface_10 × 20, respectively. d) $A_{f,\,glob}$ and $A_{f,\,local}$ as φ_H varies. Scale bars 2 mm.

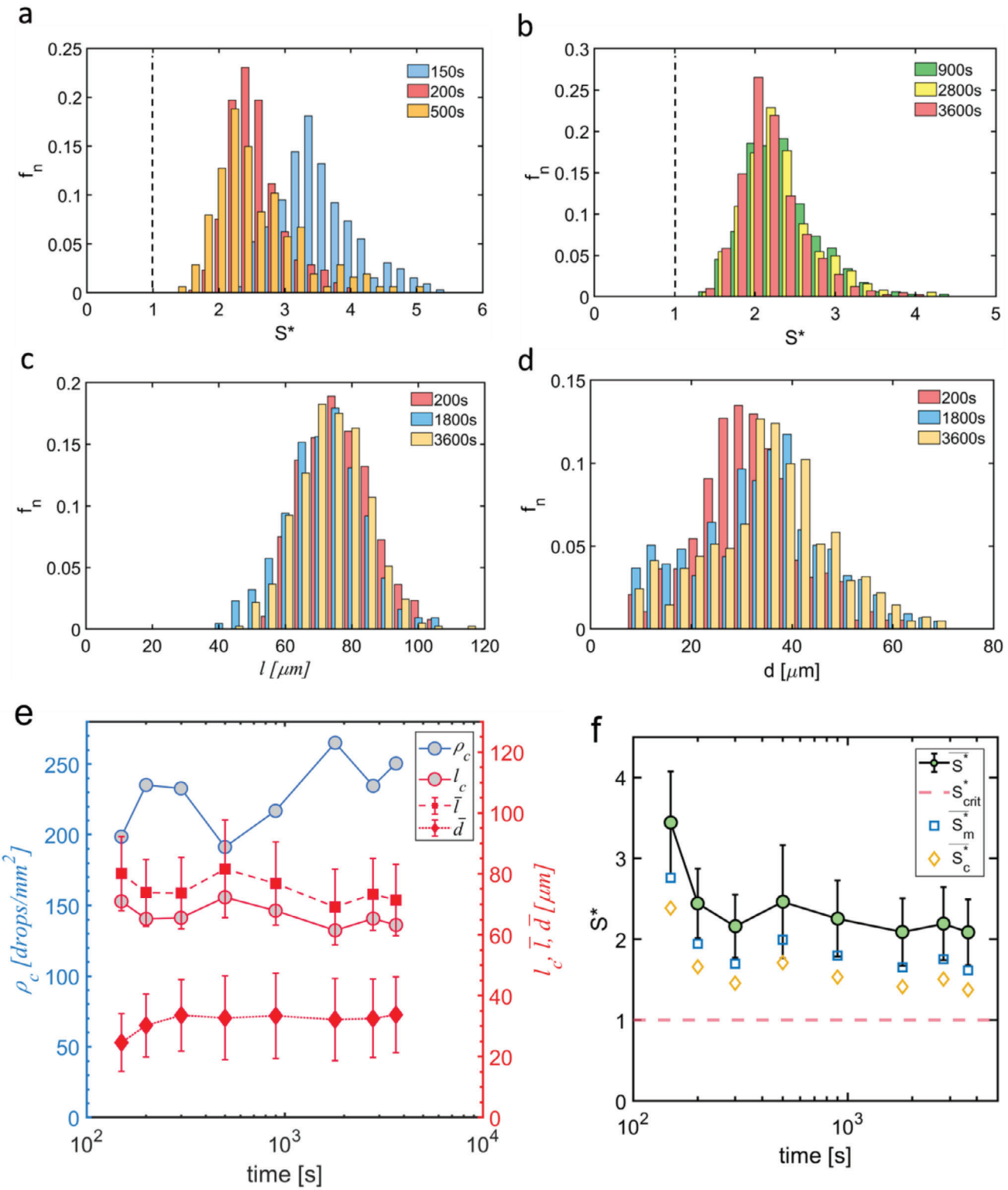

Figure 10. Normalized frequency f_n of a,b) the bridging parameter S^* (bin size 0.2) and of c) the centers distance l (bin size 5 μm) calculated as the average among the six nearest neighbors of each droplet. d) Normalized frequency f_n of the droplet diameter d (bin size 3 μm). The times are referred to the beginning of the experiment. e) ρ_c, l_c (calculated as $\sqrt{1/\rho_c}$) and the means ($\bar{l}$ and $\bar{d}$) with standard deviations of the l and d distributions. f) Mean, $\overline{S^*}$, and standard deviation of the S^*distributions. There are no droplets that satisfy the condition $S^* < S^*_{crit} = 1$ and indeed the ice-bridging in frustrated. The estimates of $\overline{S^*}$, $\overline{S^*}_m$ and $\overline{S^*}_c$, are plotted for comparison. All the data are obtained by analyzing the droplets on Surface_10 × 20 in a field of view of area 1280 × 12 800 ϵm^2.

Also, the distance distributions between the droplet centers (l) and droplet diameters (d) are steady (Figure 10c,d). The number of drops per unit area (Figure 10e) becomes quite stationary after ≈10 min and oscillates in the range 210–260 drops mm^{-2}. We see that l_c, calculated as $\sqrt{1/\rho_c}$, gives an acceptable estimate of the droplet centers distance averaged among the six nearest neighbors for each droplet ($\bar{l}$). In particular, the trend over time is the same and $\bar{l}/l_c$ ~1.12. The mean diameter $\bar{d}$ is also steady.

Finally, Figure 10f shows a steady mean of S^*, $\overline{S^*}$, relative to the distributions in Figure 10a,b. However, the approximate parameters that one can calculate as $\overline{S^*}_m \approx (\bar{l} - \bar{d}/2)/\bar{d}$ or $\overline{S^*}_c \approx (l_c - \bar{d}/2)/\bar{d}$, underestimate $\overline{S^*}$ by a relative error of −21% and −32%, respectively. Therefore, although the time trend is consistent, it is preferable to compute $\overline{S^*}$ from its real distribution.

From the point of view of surfaces that improve heat exchange by condensation, where small droplets are preferred, the distribution of droplet diameters (Figure 10d) is worthy of note, as it can be strictly controlled by the self-ejection diameter (≈28 µm for Surface_10 × 20) which is a designable parameter.

4. Perspective and Conclusion

We have shown that single droplet self-ejection delays frost propagation and overcomes the performance of the state of the art surfaces of up to one order of magnitude. On the most performing surfaces, where self-ejection is predominant, frost propagation by successful ice bridges is completely frustrated ($S^* > 1$ for all the droplets) and the frost propagates with velocities in the range 0.4–1.2 ϵm s^{-1}, 3–11 times slower than the state of art surfaces. The formation of large dry areas by drops evaporation yields a final frost coverage of 20–50% at the sample center and of 41–68% over the entire sample because of edge effects.

We also related both the self-ejection percentage and the ν_{frost} to the cone heads area percentage, φ_H. The smaller the φ_H, the larger the $\%_{s-ej}$ and the smaller the ν_{frost}. The observed trends suggests that ideal cones ($\varphi_H \to 0$) would provide $\%_{s-ej} = 100\%$ and reduce ν_{frost} even more. However, the limit case ($\varphi_H = 0$) requires confirmation with additional experimental and theoretical studies because the top meniscus could incorporate the cone heads and change the fate of the droplet.

We anticipate surface performance ($\%_{s-ej}$, ν_{frost}, and A_{frost}) to vary with T_{surf} and s. Indeed, these experimental parameters govern the distribution of condensation droplets and the growth rate of individual bridges. Future studies will explore this direction to identify potential regime shifts (from predominant self-ejection to predominant CICDJ) and determine the threshold conditions where self-ejection provides advantages.

Regarding the materials used, manufacturing on silicon with precise tuning of size and tapering served to prove the concept of self-ejection and its anti-frosting effect. Future works will be oriented on the realization of conical microstructures on materials commonly used for heat exchangers such as aluminium, which already offers the great advantage of an easy and scalable nanostructuring, or on soft polymers, intrinsically hydrophobic, which would eliminate the fragile silane layer.

Having shown here that the higher the $\%_{s-ej}$, the lower the ν_{frost}, it is advisable to reduce φ_H as much as possible because it maximizes the $\%_{s-ej}$. It is implied that, assuming that certain vertical pillars or vertical grooves enable self-ejection, tapered structures would have an advantage compared to vertical ones in terms of bending strength. At the same small φ_H, vertical structures imply lower bending strength than cones that indeed have maximal cross section where bending is maximal. Further, it is shown that inserted pinning sites[40,41] are not essential to enable self-ejection in-between cones of various sizes and pitch, which greatly facilitates manufacturing. Future studies will document and analyze the effect of different dynamic angles and of tapering on self-ejection velocity up to the limits after which self-ejection is inhibited.

In conclusion, self-ejection promises enhancements also in other fields of application where CICDJ has already provided improvements, such as condensation heat transfer, water harvesting and self-cleaning among others.

Supporting Information

Supporting Information is available from the Wiley Online Library or from the author.

Acknowledgements

The authors kindly thank Alberto Bellin, Luigi Fraccarollo and Fabio Sartori (University of Trento, Italy) who lent the Phantom camera and the Micro Nano Facility technical staff (FBK, Trento, Italy) for support in the fabrication. The study was supported by the European Commission under the FET Open "Boheme" grant no. 863179.

Conflict of Interest

The authors declare no conflict of interest.

Author Contributions

N.G.D. and A.B. designed the study and fabricated the surfaces. N.G.D. tested the surfaces, interpreted the data and wrote the manuscript. A.B. and N.M.P. discussed the data and edited the manuscript. A.B. and N.M.P. supervised the research.

Data Availability Statement

The data that support the findings of this study are available in the supplementary material of this article.

Keywords

anti-frosting, condensation frosting, droplet jumping, micro and nano fabrication, self-ejection

Received: September 11, 2023
Revised: December 13, 2023
Published online:

[1] M. Rafati Nasr, M. Fauchoux, R. W. Besant, C. J. Simonson, *Renew. Sustain. Energy Rev.* **2014**, *30*, 538.

[2] D. L. Da Silva, C. Melo, C. J. L. Hermes, *Appl. Therm. Eng.* **2017**, *111*, 1060.
[3] Y. Xia, Y. Zhong, P. S. Hrnjak, A. M. Jacobi, *Int. J. Refrig.* **2006**, *29*, 1066.
[4] F. T. Lynch, A. Khodadoust, *Prog. Aerosp. Sci.* **2001**, *37*, 669.
[5] A. J. Mahvi, K. Boyina, A. Musser, S. Elbel, N. Miljkovic, *Int. J. Heat Mass Transf.* **2021**, *172*, 121162.
[6] K. Li, D. Xia, S. Luo, Y. Zhao, R. Tu, X. Zhou, H. Zhang, L. Su, *Appl. Therm. Eng.* **2022**, *201*, 117766.
[7] M. B. Bragg, A. P. Broeren, L. A. Blumenthal, *Prog. Aerosp. Sci.* **2005**, *41*, 323.
[8] R. A. Kent, D. Andersen, P.-Y. Caux, S. Teed, *Environ. Toxicol.* **1999**, *14*, 481.
[9] Z. Goraj, 24th Congress of International Council of the Aeronautical Sciences, **2004**.
[10] Q. Su, S. Chang, Y. Zhao, H. Zheng, C. Dang, *Appl. Therm. Eng.* **2018**, *130*, 528.
[11] L. Oberli, D. Caruso, C. Hall, M. Fabretto, P. J. Murphy, D. Evans, *Adv. Colloid Interface Sci.* **2014**, *210*, 47.
[12] T. Maitra, M. K. Tiwari, C. Antonini, P. Schoch, S. Jung, P. Eberle, D. Poulikakos, *Nano Lett.* **2014**, *14*, 1106.
[13] Z. Zuo, X. Song, R. Liao, X. Zhao, Y. Yuan, *Int. J. Heat Mass Transf.* **2019**, *133*, 119.
[14] P. Eberle, M. K. Tiwari, T. Maitra, D. Poulikakos, *Nanoscale* **2014**, *6*, 4874.
[15] S. Nath, J. B. Boreyko, *Langmuir* **2016**, *32*, 8350.
[16] H. Jo, K. W. Hwang, D. Kim, M. Kiyofumi, H. S. Park, M. H. Kim, H. S. Ahn, *Sci. Rep.* **2015**, *5*, 9901.
[17] R. Enright, N. Miljkovic, A. Al-Obeidi, C. V. Thompson, *Langmuir* **2012**, *28*, 10352.
[18] J. Guadarrama-Cetina, A. Mongruel, W. González-Viñas, D. Beysens, *EPL* **2013**, *101*, 16009.
[19] X. Chen, R. Ma, H. Zhou, X. Zhou, L. Che, S. Yao, Z. Wang, *Sci. Rep.* **2013**, *3*, 2515.
[20] K. K. Varanasi, T. Deng, J. D. Smith, M. Hsu, N. Bhate, *Appl. Phys. Lett.* **2010**, *97*, 234102.
[21] T. M. Schutzius, S. Jung, T. Maitra, P. Eberle, C. Antonini, C. Stamatopoulos, D. Poulikakos, *Langmuir* **2015**, *31*, 4807.
[22] S. Chavan, D. Park, N. Singla, P. Sokalski, K. Boyina, N. Miljkovic, *Langmuir* **2018**, *34*, 6636.
[23] S. Nath, S. F. Ahmadi, J. B. Boreyko, *Soft Matter* **2020**, *16*, 1156.
[24] J. B. Boreyko, C. P. Collier, *ACS Nano* **2013**, *7*, 1618.
[25] C. Lv, P. Hao, Z. Yao, Y. Song, X. Zhang, F. He, *Appl. Phys. Lett.* **2013**, *103*, 021601.
[26] F.-C. Wang, F. Yang, Y.-P. Zhao, *Appl. Phys. Lett.* **2011**, *98*, 053112.
[27] M. D. Mulroe, B. R. Srijanto, S. F. Ahmadi, C. P. Collier, J. B. Boreyko, *ACS Nano* **2017**, *11*, 8499.
[28] P. Lecointre, T. Mouterde, A. Checco, C. T. Black, A. Rahman, C. Clanet, D. Quéré, *Phys. Rev. Fluids* **2019**, *4*, 24.
[29] J. Wasserfall, P. Figueiredo, R. Kneer, W. Rohlfs, P. Pischke, *Phys. Rev. Fluids* **2017**, *2*, 123601.
[30] Y. Shen, M. Jin, X. Wu, J. Tao, X. Luo, H. Chen, Y. Lu, Y. Xie, *Appl. Therm. Eng.* **2019**, *156*, 111.
[31] G. Zhao, G. Zou, W. Wang, R. Geng, X. Yan, Z. He, L. Liu, X. Zhou, J. Lv, J. Wang, *Soft Matter* **2020**, *16*, 4462.
[32] F. Chu, Y. Lin, X. Yan, X. Wu, *Energy Build.* **2020**, *225*, 110315.
[33] L. Li, Y. Lin, K. F. Rabbi, J. Ma, Z. Chen, A. Patel, W. Su, X. Ma, K. Boyina, S. Sett, D. Mondal, N. Tomohiro, F. Hirokazu, N. Miljkovic, *ACS Appl. Mater. Interfaces* **2021**, *13*, 43489.
[34] A. Kim, C. Lee, H. Kim, J. Kim, *ACS Appl. Mater. Interfaces* **2015**, *7*, 7206.
[35] Z. Zuo, R. Liao, X. Zhao, X. Song, Z. Qiao, C. Guo, A. Zhuang, Y. Yuan, *Appl. Therm. Eng.* **2017**, *110*, 39.
[36] G. Zhao, G. Zou, W. Wang, R. Geng, X. Yan, Z. He, L. Liu, X. Zhou, J. Lv, J. Wang, *ACS Appl. Mater. Interfaces* **2020**, *12*, 7805.
[37] J. B. Boreyko, R. R. Hansen, K. R. Murphy, S. Nath, S. T. Retterer, C. P. Collier, *Sci. Rep.* **2016**, *6*, 19131.
[38] S. F. Ahmadi, S. Nath, G. J. Iliff, B. R. Srijanto, C. P. Collier, P. Yue, J. B. Boreyko, *ACS Appl. Mater. Interfaces* **2018**, *10*, 32874.
[39] N. G. D. Novo, A. Bagolini, N. M. Pugno, *ACS Nano*, https://doi.org/10.48550/arXiv.2306.17635.
[40] X. Yan, Y. Qin, F. Chen, G. Zhao, S. Sett, M. J. Hoque, K. F. Rabbi, X. Zhang, Z. Wang, L. Li, F. Chen, J. Feng, N. Miljkovic, *ACS Nano* **2020**, *14*, 12796.
[41] L. Stendardo, A. Milionis, G. Kokkoris, C. Stamatopoulos, C. S. Sharma, R. Kumar, M. Donati, D. Poulikakos, *Langmuir* **2023**, *39*, 1585.
[42] N. S. Saadi, L. B. Hassan, T. Karabacak, *Sci. Rep.* **2017**, *7*, 7158.
[43] W. V. D. A. Vermilyea, *Trans. Faraday Soc* **1969**, *65*, 561.
[44] D. A. Vermilyea, W. Vedder, *Trans. Faraday Soc.* **1970**, *66*, 2644.
[45] F. K. Crundwell, *ACS Omega* **2017**, *2*, 1116.
[46] I. Arganda-Carreras, V. Kaynig, C. Rueden, K. W. Eliceiri, J. Schindelin, A. Cardona, H. Sebastian Seung, *Bioinformatics* **2017**, *33*, 2424.
[47] M. Haeri, M. Haeri, *J. Open Res. Softw.* **2015**, *3*, 2.
[48] D. Seo, S. Oh, B. Moon, H. Kim, J. Kim, C. Lee, Y. Nam, *Int. J. Heat Mass Transf.* **2019**, *128*, 217.
[49] Y. Shen, H. Zou, S. Wang, *Langmuir* **2020**, *36*, 13563.
[50] L. Hauer, W. S. Y. Wong, A. Sharifi-Aghili, L. Kondic, D. Vollmer, *Phys. Rev. E* **2021**, *104*, 044901.
[51] S. Jung, M. K. Tiwari, N. V. Doan, D. Poulikakos, *Nat. Commun.* **2012**, *3*, 615.
[52] A. Aili, H. Li, M. H. Alhosani, T. Zhang, *ACS Appl. Mater. Interfaces* **2016**, *8*, 21776.
[53] K. G. Libbrecht, *Snow Cryst* **2021**.
[54] Y. Hu, R. Li, X. Zhang, Y. Zhu, H.-Y. Nie, *Surface Eng.* **2019**, *36*, 589.
[55] B. K. Tudu, A. Kumar, B. Bhushan, *A.Mathematical, Phys. and Engineering Sci.* **2018**, *377*, 20180272.
[56] X. Ma, Y. Wang, H. Wu, Y. Wang, Y. Yang, Efficient water scavenging by cooling superhydrophobic surfaces to obtain jumping water droplets from air. Scientific Reports, **2019**, *9*, https://doi.org/10.1038/s41598-019-50199-9.
[57] M. Balordi, G. Santucci de Magistris, C. Chemelli, A Novel Simple Anti-Ice Aluminum Coating: Synthesis and In-Lab Comparison with a Superhydrophobic Hierarchical Surface. Coatings, **2020**, *10*, 111.
[58] L. Li, Y. Lin, K. F. Rabbi, J. Ma, Z. Chen, A. Patel, W. Su, X. Ma, K. Boyina, S. Sett, D. Mondal, N. Tomohiro, F. Hirokazu, N. Miljkovic, *ACS Appl. Mater. Interfaces* **2021**, *13*, 43489.
[59] A. Kim, C. Lee, H. Kim, J. Kim, *ACS Appl. Mater. Interfaces* **2015**, *7*, 7206.

ADVANCED MATERIALS INTERFACES
Open Access

Supporting Information

for *Adv. Mater. Interfaces*, DOI 10.1002/admi.202300759

Ice-Bridging Frustration by Self-Ejection of Single Droplets Results in Superior Anti-Frosting Surfaces

Nicolò G. Di Novo, Alvise Bagolini* and Nicola M. Pugno**

Supplementary information of "Ice-bridging frustration by self-ejection of single droplets results in superior anti-frosting surfaces"

Nicolò G. Di Novo[1,2,*], Alvise Bagolini[2,*], Nicola M. Pugno[1,3,*]

[1] *Laboratory of Bioinspired, Bionic, Nano, Meta, Materials & Mechanics, Department of Civil, Environmental and Mechanical Engineering, University of Trento, Via Mesiano, 77, 38123 Trento, Italy*
[2] *Sensors and Devices Center, Bruno Kessler Fundation, Via Sommarive 18, 38123 Trento*
[3] *School of Engineering and Materials Science, Queen Mary University of London, Mile End Road, London E1 4NS, United Kingdom*
[*] *Corresponding authors*

S1. Microstructures after t-RIE

In Figure S1, there is an example of microstructures produced by the t-RIE step. The isotropic etching component leads to etching under the hard mask and tapering.

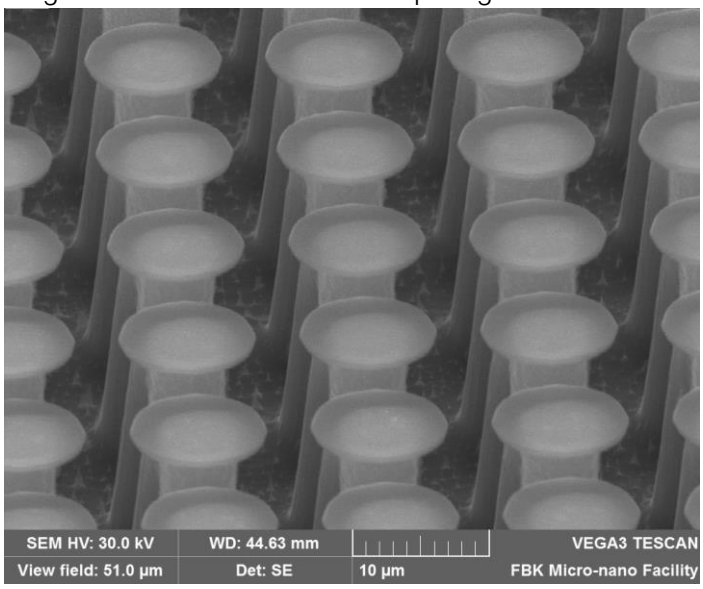

Figure S1. SEM image of Surface_10x13, tilt angle 60°, after the t-RIE step.

S2. Tapering

In some cases, the tapering is not constant over the entire height of the microcones: up to about three fourths from the bottom the tapering is constant (and it is the one reported in Table 1) while in the remaining upper part the pillar gradually becomes straight. The methodology for tapering angle (β) calculation is shown in Figure S2. With the diameter of the base (D), of the head (d_h), the projected height of the cone (c, the height observed with the SEM), and the SEM plate tilt angle (α) the real tapering is expressed in Eq. S1.

$$\beta = \tan^{-1}\left(\frac{D - d_h}{2\frac{c}{\sin\alpha}}\right) \tag{S1}$$

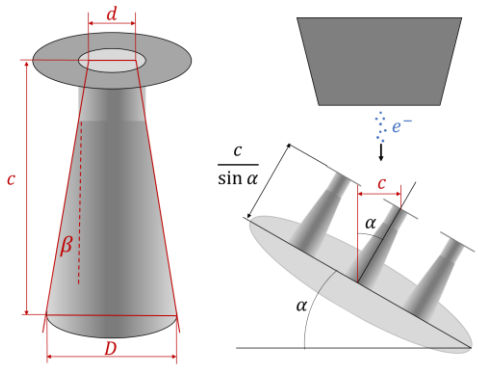

Figure S2. Illustration of SEM image analysis for tapering angle calculation.

S2. Supplementary videos

- Supplementary video 1.
  Surface_10x13 at T= 1 °C and in a atmosphere with saturation ratio equal to 2.8. Placed vertically so that droplets do not re-fall on the surface. For the high frame rate recording of droplets self-ejection from the microstructures of the sample edges we used T above 0°C to avoid icing, more likely because of the vicinity with the thermal paste. This stands also for Supplementary videos 2-5. Side-view recording done with the Phantom camera. Frame rate: 66 000.

- Supplementary video 2.
  Surface_60x80 at T= 1 °C and in a atmosphere with saturation ratio equal to 2.8. Placed vertically. Side-view recording done with the Phantom camera. Frame rate: 10 000.

- Supplementary video 3.
  Surface_15x20 at T= 1 °C and saturation ratio 2.8. Placed vertically. Side-view recording done with the Phantom camera. Frame rate: 80 000.

- Supplementary video 4.
  Surface_60x80 at T= 1 °C and saturation ratio 2.8. Placed vertically. Side-view recording done with the Phantom camera. Frame rate: 8 860.

- Supplementary video 5.
  Surface_60x80 at T= 1 °C and saturation ratio 2.8. Placed horizontally. Side-view recording done with the Phantom camera. Frame rate: 4 420.

- Supplementary video 6.
  Surface_15x20p at T= -11 °C and saturation ratio 2.8. Placed vertically. Top-view recording done with the Dinolite microscope, accelerated 32 times and cropped.

- Supplementary video 7.
  Surface_30x40 at T= -11 °C and saturation ratio 2.8. Placed vertically. Top-view recording done with the Dinolite microscope, accelerated 64 times and cropped.

- Supplementary video 8.
  Surface_10x20 at T= -11 °C and saturation ratio 2.8. Placed vertically. Top-view recording done with the Dinolite microscope, accelerated 256 times.

  Supplementary video 9.Surface_10x15 at T= -11 °C and saturation ratio 2.8. Placed vertically. Top-view recording done with the Dinolite microscope, accelerated 256 times.